THE ASTROPHYSICAL JOURNAL, 402:710–720, 1993 January 10

THE HYDROGEN LYMAN-ALPHA EMISSION OF CAPELLA

THOMAS R. AYRES[1]
Center for Astrophysics and Space Astronomy, University of Colorado, Campus Box 389, Boulder, CO 80309-0389
AND
A. BROWN, K. G. GAYLEY, AND JEFFREY L. LINSKY[2]
Joint Institute for Laboratory Astrophysics, University of Colorado and National Institute of Standards and Technology, Boulder, CO 80309-0440
Received 1992 June 8; accepted 1992 July 28

ABSTRACT

We describe the hydrogen Lyα emission of the spectroscopic binary Capella (G8 III + G0 III) recorded at 0.1 Å resolution by the *International Ultraviolet Explorer*. The overt changes in the composite line shape with orbital phase are controlled by the active G0 III star and permit a dissection of the stellar components despite the obliteration of the central portion of the profile by atomic hydrogen and deuterium absorption along the 12.5 pc sightline. The Lyα line shape of the active G0 III star is surprisingly asymmetric and possibly is variable. Both characteristics suggest a stellar wind of moderate excitation (2×10^4–1×10^5 K), a key component of the coronal evolution scenario of Simon & Drake for the Hertzsprung-gap giants.

In a companion paper Linsky et al. use the intrinsic Lyα line shape of Capella to derive the interstellar hydrogen column density and the cosmologically significant D/H ratio based on a comparison with a 0.015 Å resolution profile obtained by the Goddard High Resolution Spectrograph of the *Hubble Space Telescope*.

Subject headings: line: profiles — stars: chromospheres — stars: individual (α Aurigae) — ultraviolet: stars

1. INTRODUCTION

On 1991 April 15 Linsky et al. (1993) recorded the chromospheric emission profile of H I λ1215 Lyα in the nearby spectroscopic binary Capella (α Aur = HD 34029; G8 III + G0 III; $P = 104$ d) using ECH-A of the *HST* Goddard High Resolution Spectrograph. The unique observation (side 1 of the GHRS failed shortly thereafter) provided for the first time a clear view of the sharp D I absorption flanking the strong depression due to interstellar atomic hydrogen in the core of the stellar emission profile.

The interstellar D I feature is of great interest because of the role played by the D/H ratio in tracing the chemical evolution of the Galaxy and the very early history of the universe. The ECH-A observation permits a precise measurement of the deuterium column along the 12.5 pc sightline to Capella. To derive an accurate isotopic ratio, however, one must also determine the atomic hydrogen column with comparable precision. This is possible through analysis of the Voigt "shoulder" of the H I Lyα absorption, but characteristics of the underlying composite emission profile must be known in order to determine an accurate value for N_H. A spectral decomposition from the single *Hubble* observation is ambiguous.

Fortunately, however, Capella has been a popular target for the *IUE* far-ultraviolet echelle mode. The 0.1 Å resolution of the *IUE* is adequate—together with the good phase coverage—to permit a reliable dissection of the observed profiles into the two stellar emission components. The decomposition in turn permits an accurate determination of the interstellar H I absorption that overlies the intrinsic profile. The analysis of the *IUE* spectra of Capella is the subject of the present paper.

[1] Guest Observer, *International Ultraviolet Explorer*.
[2] Staff Member, Quantum Physics Division, National Institute of Standards and Technology.

2. OBSERVATIONS AND REDUCTIONS

Capella should be an ideal light source for a study of the interstellar hydrogen absorption. The binary is the brightest of the nearby Lyα emission stars. The fast-rotating G0 III star dominates the chromospheric and higher-excitation emissions of the system (Ayres & Linsky 1980), and its line fluxes are surprisingly stable, showing no measurable modulations over rotational time scales (Ayres 1984, 1991a). The properties of the system are well-determined (Bagnuolo & Sowell 1988; Batten, Hill, & Lu 1991). The large rotational broadening, accurately determined orbit, and flux stability suggest that the chromospheric line shapes should be smooth, predictable, and invariable.

Nevertheless the red/blue peak ratio of the GHRS Lyα profile was significantly different from published *IUE* profiles (e.g., Ayres, Schiffer, & Linsky 1983). Variability of the Lyα emission was deemed unlikely for the reasons given above. When an exhaustive check of the GHRS calibration procedures revealed no anomalies that could account for the discrepant red/blue peak ratio, suspicion turned to the *IUE* data. A reconnaissance of SWP-HI spectra of Capella in the *IUE* Archives revealed surprising variability in the profile shapes and a disturbing inconsistency between the adjacent echelle orders ($m = 113$ and 114) in which Lyα appears. We therefore conducted a careful examination of the entire collection of SWP-HI spectra of the well-known binary.

2.1. *Catalog of IUE Observations*

One-hundred-twenty SWP echellograms of Capella are listed in the Merged Catalog of Observations (through 1992 February). The earliest dates to 1978 April, and the most recent was obtained 1992 February 21 in support of an EUV sounding-rocket flight (Green et al. 1992). The spectrum closest in time to the GHRS ECH-A observation was taken 1991

TABLE 1

CATALOG OF OBSERVATIONS

SWP Number (1)	Aperture (2)	t_{exp} (minutes) (3)	J.D. 2,443,000+ (4)	Orbital Phase (5)	Observer (6)	Raw Fluxes (DN) 113/114/BKG (7)
01304.....	S	16	0602.0	0.50	Linsky	89/49/18
01305.....	S	120	0602.1	0.50	Linsky	250/149/35
01454.....	S	90	0630.3	0.78	Linsky	214/131/72
02299.....	L	180	0735.9	0.79	Linsky	255/255/64
02352.....	S	60	0742.1	0.85	Linsky	189/110/35
07104.....	L	19	1184.0	0.10	Black	155/86/25
08178.....	L	30	1305.4	0.27	Ayres	179/103/23
08179.....	S	60	1305.4	0.27	Ayres	237/116/38
08181.....	L	30	1305.5	0.27	Ayres	191/124/25
08182.....	L	30	1305.6	0.27	Ayres	208/116/25
08183.....	L	30	1305.6	0.27	Ayres	190/114/24
08626.....	L	10	1331.3	0.52	Schiffer	81/51/17
08627.....	L	30	1331.4	0.52	Schiffer	178/103/22
08628.....	L	25	1331.4	0.52	Schiffer	160/88/21
08629.....	L	25	1331.4	0.52	Schiffer	156/88/21
08630.....	L	25	1331.5	0.52	Schiffer	160/87/20
08631.....	L	25	1331.5	0.52	Schiffer	153/96/21
08632.....	L	10	1331.6	0.52	Schiffer	78/53/18
08832.....	L	30	1356.3	0.76	Schiffer	187/117/25
08833.....	L	30	1356.3	0.76	Schiffer	193/124/24
08834.....	L	30	1356.4	0.76	Schiffer	184/108/24
08835.....	L	30	1356.4	0.76	Schiffer	186/110/24
08836.....	L	30	1356.5	0.76	Schiffer	181/110/24
08837.....	L	30	1356.5	0.76	Schiffer	190/104/22
08838.....	L	30	1356.6	0.76	Schiffer	186/99/21
11028[a].....	L	60	1616.6	0.26	Simon	253/172/32
11030.....	L	10	1616.6	0.26	Simon	85/62/18
11032[a].....	L	60	1616.7	0.26	Simon	254/189/33
11033[a].....	L	60	1616.7	0.26	Simon	254/168/38
13446[a].....	L	60	1673.4	0.80	Seab	253/168/39
13447.....	L	10	1673.4	0.80	Seab	80/70/19
13468.....	L	60	1676.4	0.83	Brugel	251/177/38
13469.....	L	10	1676.4	0.83	Brugel	86/61/18
13488.....	L	60	1678.4	0.85	Brugel	251/148/29
13489.....	L	12	1678.4	0.85	Brugel	96/52/17
13535.....	L	60	1683.4	0.90	Mullan	251/160/37
13536.....	L	10	1683.5	0.90	Mullan	86/49/19
13558.....	L	10	1687.4	0.94	Ayres	83/66/20
13560.....	L	25	1687.5	0.94	Ayres	160/105/28
13578.....	L	50	1689.5	0.96	Simon	249/161/25
13579.....	L	10	1689.5	0.96	Simon	93/50/17
13597.....	L	50	1691.5	0.98	Simon	253/163/55
13598.....	L	10	1691.6	0.98	Simon	97/54/23
13610.....	L	10	1693.3	0.00	Stencel	86/54/19
13611.....	L	50	1693.3	0.00	Stencel	251/151/39
13625.....	L	30	1695.3	0.01	Stencel	195/104/28
13644.....	L	10	1697.3	0.03	Stencel	93/61/23
13645.....	L	50	1697.4	0.03	Stencel	249/160/49
13656.....	L	60	1699.5	0.05	Stencel	254/167/43
13657.....	L	10	1699.5	0.05	Stencel	92/66/20
13672.....	L	60	1701.4	0.07	Basri	255/179/47
13673.....	L	10	1701.5	0.07	Basri	82/66/20
13691.....	L	60	1704.5	0.10	Wing	254/172/42
13692.....	L	10	1704.5	0.10	Wing	93/63/19
13700.....	L	30	1706.4	0.12	Wing	188/104/20
13721.....	L	60	1710.4	0.16	Stencel	253/161/34
13722.....	L	10	1710.4	0.16	Stencel	82/52/18
13741[a].....	L	60	1712.4	0.18	Ayres	251/174/33
13742.....	L	10	1712.4	0.18	Ayres	80/56/19
13756[a].....	L	60	1714.5	0.20	Ayres	253/180/34
13757.....	L	10	1714.5	0.20	Ayres	71/52/17
13773[a].....	L	60	1716.4	0.22	Ayres	255/191/38
13774.....	L	10	1716.4	0.22	Ayres	81/57/21
13791[a].....	L	60	1718.5	0.24	Ayres	255/205/60
13792.....	L	10	1718.6	0.24	Ayres	77/51/17
13808[a].....	L	30	1720.5	0.26	Ayres	178/102/20
13821.....	L	10	1722.4	0.27	Baroff	85/57/22
13823[a].....	L	25	1722.5	0.28	Baroff	176/105/36
13825[a].....	L	60	1722.5	0.28	Baroff	253/169/29
13842[a].....	L	40	1724.3	0.29	Ayres	229/154/41

TABLE 1—*Continued*

SWP Number (1)	Aperture (2)	t_{exp} (minutes) (3)	J.D. 2,443,000+ (4)	Orbital Phase (5)	Observer (6)	Raw Fluxes (DN) 113/114/BKG (7)
13843.....	L	10	1724.3	0.29	Ayres	76/62/21
16660.....	S	240	2058.1	0.50	Ayres	255/148/40
18779.....	L	15	2315.8	0.98	Ayres	101/60/19
18781.....	L	80	2315.9	0.98	Ayres	255/191/32
18786.....	L	22.5	2316.8	0.99	Ayres	161/96/29
18788.....	L	97	2316.9	0.99	Ayres	255/229/45
18792.....	L	22.5	2317.8	0.00	Ayres	170/92/26
18794.....	L	137	2317.9	0.00	Ayres	255/253/68
18799.....	L	22.5	2318.8	0.01	Ayres	140/85/22
18801.....	L	108	2318.9	0.01	Ayres	255/247/41
18803.....	L	22.5	2319.8	0.02	Ayres	167/86/21
18805.....	L	106	2319.9	0.02	Ayres	255/244/38
18810.....	L	22.5	2320.8	0.03	Ayres	150/78/20
18812.....	L	148	2320.9	0.03	Ayres	255/255/70
21200.....	L	15	2608.0	0.79	Ayres	138/108/68
21201[a].....	L	60	2608.1	0.79	Ayres	253/190/75
27119[a].....	L	90	3385.4	0.26	Ayres	255/190/33
27120[a].....	L	90	3385.5	0.26	Ayres	255/201/41
27121.....	S	180	3385.7	0.26	Ayres	228/136/54
27122.....	S	30	3385.8	0.27	Ayres	98/81/52
27124.....	L	15	3385.9	0.27	Ayres	108/69/28
27445[a].....	L	90	3435.2	0.74	Ayres	255/188/34
27446[a].....	L	90	3435.3	0.74	Ayres	255/215/64
27447.....	S	45	3435.4	0.74	Ayres	141/99/59
27448.....	S	90	3435.5	0.74	Ayres	212/169/120
27452.....	L	15	3435.7	0.75	Ayres	121/104/53
28058.....	L	35	3520.3	0.56	Ayres	208/147/46
28063.....	L	35	3520.5	0.56	Ayres	207/147/46
28064.....	L	35	3520.6	0.56	Ayres	213/127/42
34164[b].....	S	120	4405.9	0.07	Murthy	...
34165[b].....	S	90	4406.0	0.07	Murthy	...
34166[b].....	S	100	4406.1	0.07	Murthy	...
34713.....	M	2 × 100	4475.4	0.74	Ayres	255/224/47
34714.....	M	2 × 100	4475.6	0.74	Ayres	255/244/50
34715.....	M	2 × 15	4475.7	0.74	Ayres	124/75/18
34716.....	M	2 × 15	4475.8	0.74	Ayres	109/68/20
34717.....	M	2 × 15	4475.8	0.74	Ayres	124/87/36
34718.....	M	2 × 15	4475.9	0.75	Ayres	117/79/23
34719.....	M	2 × 30	4475.9	0.75	Ayres	172/95/25
35265.....	M	2 × 15	4532.5	0.29	Ayres	122/66/18
35266.....	M	2 × 15	4532.5	0.29	Ayres	111/64/18
35269.....	M	2 × 30	4532.7	0.29	Ayres	191/104/25
35271.....	M	2 × 14	4532.8	0.29	Ayres	112/63/18
35276.....	M	2 × 100	4533.3	0.30	Ayres	255/215/50
35277.....	M	2 × 100	4533.4	0.30	Ayres	255/248/52
35605.....	M	2 × 30	4579.5	0.74	Ayres	169/98/25
35609.....	M	2 × 30	4580.5	0.75	Ayres	171/101/27
40567.....	L	14.5	5268.7	0.37	Rawley	97/50/15
43967[c].....	L	30	5664.5	0.17	Ayres	...
43974[c].....	L	30	5665.5	0.18	Ayres	...
43983[c].....	L	30	5666.5	0.19	Ayres	...
43991[c].....	L	30	5667.5	0.20	Ayres	...
43992.....	L	30	5667.5	0.20	Ayres	149/79/19
44037[c].....	L	30	5674.3	0.27	Ayres	...
44038.....	L	30	5674.4	0.27	Ayres	153/78/16

NOTES.—All exposures in high-dispersion (echelle) mode. Col. (2): L = large aperture; S = small aperture; M = multiple exposure in large aperture. Col. (3): exposure time in minutes. Col. (5): ephemeris cited by Ayres 1988; $\phi = 0$ is the conjunction with the G8 III star in front. Col. (6): as listed in Merged Log. Col. (7): peak fluxes for Lyα features in orders 113 and 114; median flux for "background" midway between the Lyα features, where BKG $\approx$ 20 corresponds to the NULL level.

[a] Images included in profile average for $\phi = 0.25 \pm 0.07$ or $\phi = 0.75 \pm 0.07$ sets.

[b] Not available in raw-image archive at National Space Sciences Data Center.

[c] Sky-background exposures, with Capella placed in LW large aperture.

January 15. Five additional exposures—in 1992 February—were of the diffuse "sky" emission in the vicinity of Capella. Table 1 summarizes the SWP-HI observations. We calculated orbital phases with the ephemeris cited by Ayres (1988): $\phi = 0$ is the conjunction with the (slightly) more massive G8 III star in front.

2.2. *Extraction and Calibration*

The standard reduction of *IUE* echelle images by the Spectral Image Processing System (IUESIPS) is adequate for many scientific applications. However, the crowded end of the echelle format where Lyα falls is particularly prone to reduction errors and merits special treatment. We therefore developed a photo-

metric linearization and spectral extraction procedure specifically for Lyα based on our previous experience with the *IUE* SWP-LO mode (Ayres et al. 1993).

2.2.1. *Image Rotation*

First we rotate the 768 × 768 raw camera frame by 51°.2 and excise a 512 × 100 subimage. The echelle pattern is roughly parallel to the long axis of the subimage (hereafter designated the "SAMPLE" direction). The subimage extends in SAMPLE from one edge of the active area of the camera target to just past the position of Lyα in $m = 114$. In the cross-dispersion direction it covers echelle orders 108 and higher. Reformatting the geometry of the image simplifies a number of the subsequent steps.

2.2.2. *Photometric Linearization*

Next we photometrically correct the subimage to a linear intensity scale by applying an "Intensity Transfer Function" to each pixel. We adopted a fourth-order polynomial representation of the ITF in DN-NULL, where DN is the telemetered 8 bit data number (i.e., 0–255) and NULL is the camera "pedestal" (the quasi-uniform ≈ 20 DN remaining on the camera target following the preparation cycle). We constructed our ITF using the series of UV-flood and NULL images from the early-1985 recalibration of the SWP camera. Further details can be found in Ayres (1993) and Ayres et al. (1993).

2.2.3. *Noise Model*

We also developed—from the same collection of UV-flood images—models of the noise properties of the Lyα region in terms of linearized intensity and SAMPLE position. At low intensities the noise has a Poisson (square root of signal) character, but at intermediate and higher exposure levels the noise becomes directly proportional to the signal, owing to the physical saturation of the camera target (Ayres 1993). In the latter regime the S/N does not improve with increasing exposure.

2.2.4. *Optimal Extraction*

We implemented an "Optimal" extraction technique like that described for *IUE* low-dispersion spectra by Kinney, Bohlin, & Neill (1991). The empirically determined cross-dispersion profile of the Optimal technique is advantageous in our Lyα investigation because it yields improved S/N compared with the IUESIPS "boxcar"; it accurately follows the short-range curvature of the spectral traces; it suppresses the contamination by emission features in the adjacent crowded echelle orders; and it provides an uncertainty for each extracted flux (as propagated from the underlying noise model).

2.2.5. *Wavelength Scale*

We dearchived 10 representative SWP-HI wavelength calibration images with camera temperatures close to that of our ITF. We selected 24 Pt II emissions in the Lyα region based on laboratory measurements of a Pt/Ne hollow-cathode lamp similar in design to the *IUE* flight lamps (Reader et al. 1990). We obtained dispersion solutions in terms of $\Delta k \equiv (m \times \lambda - k)/k$, where $k = 137{,}800$ is the echelle grating constant. A third-order polynomial in SAMPLE accurately fitted the group of calibration lines with an rms deviation of less than 1 pixel (≈ 30 mÅ).

2.2.6. *Background Correction*

Proper compensation for the off-spectrum background is critical to the successful reduction of *IUE* echellograms. In addition to the quasi-uniform fogging due to particle radiation, localized sources of enhanced background can result from grating-scattered light and diffuse Lyα sky emission through the large aperture. The IUESIPS samples the background in the interorder zones flanking the target echelle order. The strategy works well for the lower orders where adjacent spectral stripes are well separated, but is unreliable at the high end of the format where the orders are crowded. For example, Si III λ1206 falls alongside the red wing of Lyα in the next higher order and can adversely affect the background pixels in the IUESIPS reduction. Our approach was to measure the background in the interorder zones flanking $m = 111$ and $m = 116$, that is, close to the Lyα features but avoiding the immediate region surrounding them.

Figure 1 depicts the photometric linearization, background correction, and Optimal extraction of one of the recent SWP-HI exposures of Capella. We also processed the five sky-background exposures from 1992 February to evaluate the diffuse Lyα emission under typical conditions. It was faint and showed little change over the 10 day period.

2.2.7. *Absolute Calibration*

An absolute flux scale is not crucial to our analysis, although the *relative* sensitivity variation across the Lyα region is important. For that purpose we utilized the DA white dwarf G191-B2B, a fundamental flux reference for the *IUE*. It has a relatively featureless spectrum, and its ultraviolet energy distribution is believed to be accurately known. We used three 1.5 hr exposures—SWP13541, SWP18217, and SWP22428—taken relatively close to the epoch of our ITF. The energy distribution of G191-B2B was kindly provided by D. Finley of the University of California at Berkeley. We did not undertake a detailed assessment of the uncertainties in the absolute calibration because the plausible range in its *slope* across the 2 Å extent of the Lyα emission is small compared with other sources of uncertainty, particularly the echelle blaze correction.

2.2.8. *Wavelength Registration*

A precise registration of the zero point of the wavelength scale is essential to the proper application of the blaze correction and to the intercomparison of spectra obtained at different orbital phases. We adjusted each *IUE* profile to the heliocentric frame by cross-correlating it against the strong interstellar D I + H I absorption trough of the GHRS profile smoothed with a 25 km s^{-1} FWHM Gaussian to the *IUE* resolution. The shape and wavelength of the absorption core should depend mostly on the heliocentric velocity of the ISM (which is constant) and minimally on the flux of the underlying emission profile (which varies with orbital phase).

2.2.9. *Active Blaze Correction*

Detailed studies of standard stars have shown that the echelle blaze constant k, which determines the wavelength of the peak of the bell-shaped sensitivity function, varies with order number m (e.g., Grady & Garhart 1989). The value appropriate to the Lyα region is poorly determined, however, because the early-type spectra of the standard stars suffer severe "order overlap" at the high end of the SWP echelle format. We thus determined an empirical value for k in the 1216 Å region by balancing the fluxes of the Lyα features in $m = 113$ and 114.

In practice, we chose a 0.7 Å bandpass in the blue wing of Lyα and a 0.5 Å bandpass in the red wing, and adjusted the

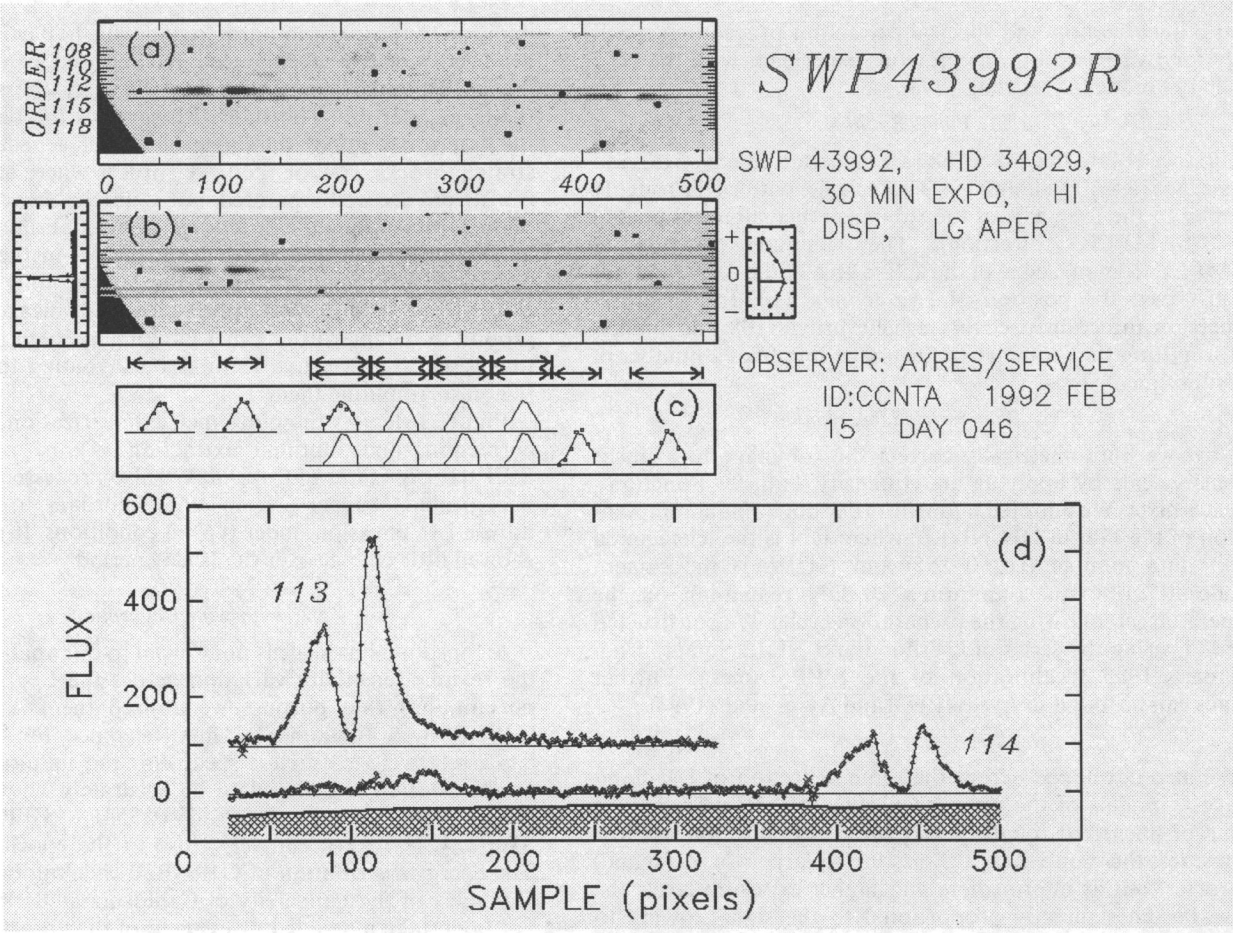

FIG. 1.—Processing scheme applied to the 120 archival SWP-HI spectra of Capella. Panel (*b*): rotated and photometrically corrected 512 × 100 subimage. The $m = 113$ Lyα feature is to the left; $m = 114$ is to the right. Dark spots indicate an unreliable photometric correction usually due to a reseau mark. The edge of the circular vidicon target is visible at the lower left of the subimage. Horizontal stripes highlight the zones astride $m = 111$ and 116 where the off-spectrum background was sampled. The two smaller plots flanking the frame depict the automatic registration of the echelle pattern. Panel (*a*): background-corrected subimage (stretched to reveal faint structure). The centroids of $m = 113$ and 114 are marked with horizontal lines. Panel (*c*): empirical cross-dispersion profiles of our realization of the "Optimal" extraction. Arrows indicate discrete wavelength intervals over which the profiles were determined (upper, $m = 113$; lower, $m = 114$). Points indicate that sufficient signal was present in the interval to determine the profile; the solid curves indicate a "default" profile established by the entire order. A rectangular ("boxcar") profile is utilized by the IUESIPS. Panel (*d*): extracted spectra for the adjacent orders (wavelength increases to right). The hatched area shows the variation of the off-spectrum background. Crosses denote fluxes flagged as unreliable (affected by a reseau, for example). Note that the Lyα profile of $m = 114$ is weaker than that of $m = 113$ and has nearly equal peak intensities: it is located at the edge of the echelle blaze, but on a more favorable area of the camera than the companion image in $m = 113$. The faint emission structure in the $m = 114$ trace near SAMPLE ≈ 150 is due partly to Si III λ1206.

grating parameter k_0 (the constant term in the parabolic expansion $k = k[m]$ proposed by Grady & Garhart 1989) to minimize the rms deviation of the total band between the $m = 113$ and 114 traces.

Before registering the wavelength scales and balancing the bandpass fluxes we subtracted from each order the diffuse Lyα emission obtained previously from the sky-background images. We performed the subtraction in the SAMPLE coordinate system so that the diffuse emission would be placed at the correct spatial position regardless of the location of the star in the large aperture at the time of observation.

For the collection of ≈40 exposures in the range 20–60 minutes we obtained $k_0 = 137{,}700 \pm 12$, which is somewhat smaller than the nominal value 137,730 (Grady & Garhart 1989). The nearly constant k_0 is encouraging because the blaze characteristics should be stable in the satellite's reference frame, which deviates from the adopted heliocentric frame only by the relatively small telluric motion (at most ±0.1 Å ≈ ±10 in units of *k*). We did not adjust the other grating constant "α," which controls the FWHM of the blaze function, because it appears to be independent of *m* and has been accurately determined from the standard-star spectra (Grady & Garhart 1989; O'Brien, Rees, & Howarth 1990).

We then recalibrated the entire collection of Capella spectra according to the average value $k_0 = 137{,}700$. We obtained generally good agreement between the Lyα profiles of the adjacent echelle orders thereby solving one of the anomalies we originally identified in the archival spectra. Nevertheless there still appeared to be significant changes over time in the Lyα red/blue peak asymmetry and overall flux. Figure 2 illustrates representative examples. The agreement with the GHRS profile is best for the *IUE* observations taken during the period 1981–1985. The most discrepant spectra—with red/blue peak ratios closer to unity—are in a series obtained in early 1980 (at $\phi = 0.27$) and the most recent observations (including a series in early 1989 at $\phi = 0.29$).

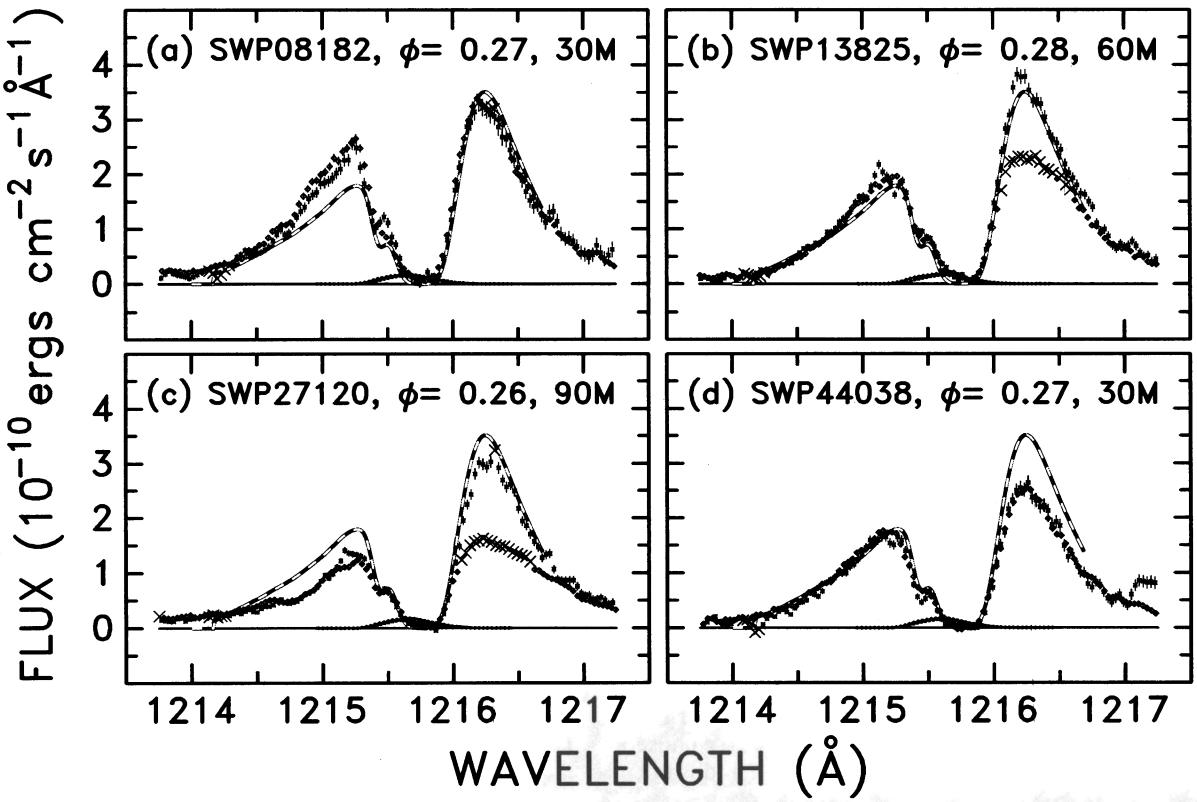

FIG. 2.—Representative calibrated spectra before correction for the secular decline in the SWP sensitivity. Fluxes (with 1 σ error bars) from $m = 113$ are plotted as diamonds; those from $m = 114$ as asterisks. Crosses flag unreliable fluxes (note overexposure of red peaks of $m = 113$ profiles in [*b*] and [*c*]). The weak emission features in the core of the stellar Lyα profile represent the correction applied for diffuse sky emission. The dashed curves are the GHRS profile ($\phi = 0.26$) smoothed to the 25 km s^{-1} *IUE* resolution. Note the discrepant red/blue peak asymmetries of the early and most recent profiles; the two intermediate epoch profiles are more *Hubble*-like. The decline in the red-peak flux from (*b*) to (*d*) very likely reflects the long-term degradation of the SWP camera. Thus the SWP44038 profile likely has an enhanced blue peak like that of SWP08182, rather than a depressed red peak.

2.2.10. *Sensitivity Degradation*

The performance of the SWP camera has been monitored carefully through long-term studies of standard stars in low dispersion. The sensitivity of the camera has declined over its 14 years of operation with the largest changes at the shorter wavelengths (Bohlin & Grillmair 1988). Unfortunately no comparable studies have been made of the echelle mode. Figure 3 illustrates the relative positions of the low- and high-resolution spectral formats. Significantly, the locations where Lyα falls in the SWP echellogram are insulated to some extent from the short-wavelength irradiation received by nearby parts of the camera, because the damaging early-type continuum

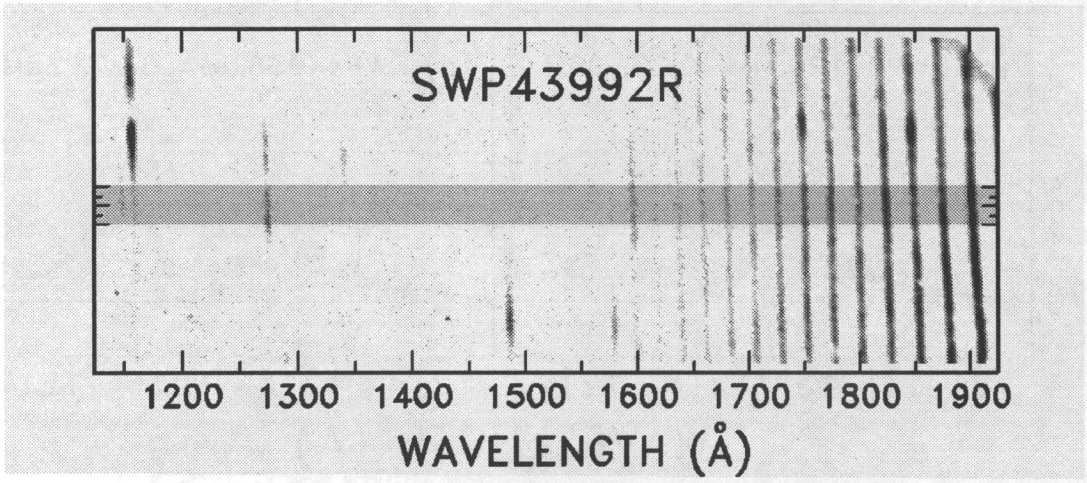

FIG. 3.—Appearance of the SWP echelle pattern in the low-dispersion reference frame. The 20 pixel wide footprint of the SWP-LO large-aperture spectrum is highlighted, and the associated wavelength scale is provided. The $m = 113$ Lyα feature falls just above the SWP-LO stripe near 1150 Å. The feature near 1480 Å below the SWP-LO stripe is C IV λ1548.2. The purpose of the comparison is to select the appropriate low-dispersion degradation curve (as a function of SWP-LO wavelength: Bohlin & Grillmair 1988) for exploring the sensitivity decline in echelle orders $m = 113$ and 114: the long-term performance of the camera has been evaluated only for the restricted area sampled by the SWP-LO mode.

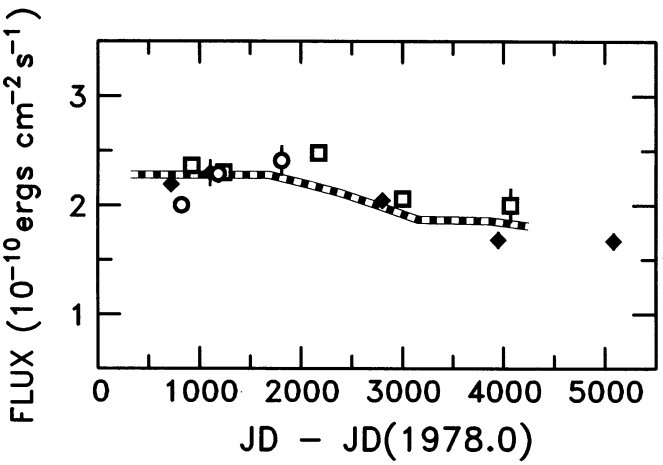

FIG. 4.—Empirical sensitivity variation of SWP camera at the location of the red peak of Lyα in $m = 114$. *Diamonds:* $\phi = 0.25$; *circles:* $\phi = 0.00$ and 0.50; and *squares:* $\phi = 0.75$. The thick-dashed curve represents our adopted sensitivity decline for the Lyα zone of $m = 114$: the low-dispersion relation reported by Bohlin & Grillmair (1988: 1155–1165 Å; see Fig. 3) *delayed by 1000 days.*

sources tend to have low fluxes in the interval 1210–1220 Å owing to interstellar H I extinction. Figure 4 illustrates the temporal variation of the apparent fluxes integrated under the red peak of the Capella Lyα emission from $m = 114$. We chose the red peak because it is well defined in wavelength and is not affected by diffuse sky emission. We chose the Lyα feature in $m = 114$ because it is from the least irradiated portion of the SWP camera. The secular decline of the Capella Lyα emission in high dispersion can be fitted by the appropriate SWP-LO curve with a time delay of ≈ 1000 days.

2.2.11. *Retrospective Comparison with IUESIPS*

After applying our new reduction to the complete set of SWP-HI images we conducted a detailed comparison with the archival material. We discovered that much of the apparent discrepancy in the IUESIPS spectra between $m = 113$ and 114 could be removed simply by the small reduction in the Grady-Garhart value of k_0 and by our post facto wavelength registration. Our new background correction, which includes compensation for the diffuse Lyα emission, provides a more realistic (i.e., *Hubble*-like) interstellar absorption core. However, these improvements could have been applied equally well to the IUESIPS-processed spectra. Our photometric correction probably is somewhat better (see Ayres 1993), if only because it is based on the careful 1985 recalibration of the SWP camera. Nevertheless the IUESIPS profiles are remarkably similar to our reductions considering the very different strategies used in the photometric correction, spectral extraction, and calibration. Figure 5 illustrates typical examples.

Our new processing did not improve the appearance of the "discrepant" set of $\phi \approx 0.25$ profiles from early in the mission (i.e., the 1980 series at $\phi = 0.27$) or those images obtained since early 1989. Thus our original motivation for developing an

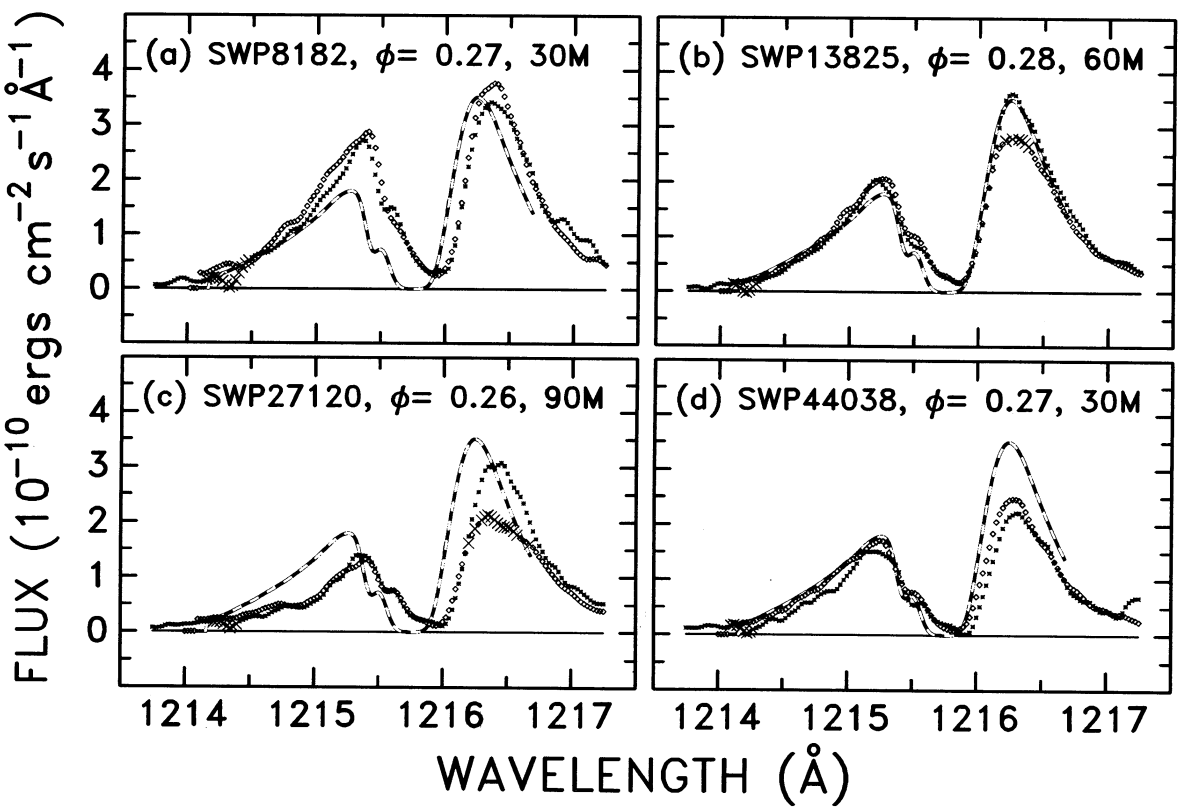

FIG. 5.—Same as Fig. 2 for the routine IUESIPS processing (although with a modified background correction). Aside from minor errors in the wavelength scales and blaze corrections, the IUESIPS profiles are remarkably similar to our independent reductions despite the very different approaches with regard to photometric linearization, extraction, and calibration. Many of the improvements we implemented could have been applied equally well to the postprocessing of the IUESIPS profiles. Nevertheless the independent reduction provided increased confidence in the reliability of the *IUE* and permitted us to reprocess the entire collection of Capella images uniformly.

independent way to process the SWP-HI images appears to have been based on the false expectation that the Capella Lyα emission should be constant. The "problem" apparently resides with the star itself, not with the *IUE*.

2.3. *Co-added Profiles at the Opposite Quadratures*

Our objective was to provide a set of reference profiles of the Lyα emission of Capella at opposite radial velocity extrema to help determine the interstellar hydrogen column density and D/H ratio in the line of sight to Capella (as described in the companion paper by Linsky et al. 1993). Given the SWP sensitivity degradation and the possible profile variability of the Capella Lyα emission we restricted the initial sample to the echellograms taken between 1980.0–1986.1, that is, prior to and immediately after the recalibration of the camera in early 1985. We included only large-aperture spectra because the small-aperture observations cannot be calibrated reliably. We also restricted our consideration to the Lyα profiles from $m = 114$ only. The blue and red peaks of Lyα in $m = 114$ are nearly equal in intensity in the raw images and thus are less affected by nonlinearities in the ITFs and by saturation in the deeper exposures. Furthermore, the effective resolution is somewhat higher (i.e., ≈ 25 km s^{-1} FWHM in $m = 114$ vs. ≈ 30 km s^{-1} in $m = 113$). We included SWP-HI images of $\gtrsim 20$ minutes exposure to ensure adequate raw signal in $m = 114$, and $\lesssim 90$ minutes to avoid overexposures. We also eliminated several observations (e.g., SWP08178 and SWP08833) for which the $m = 114$ profile was corrupted by an extended cosmic-ray "comet."

We co-added the selected profiles in two groups within ± 0.07 cycles of the opposite orbital quadratures ($\phi = 0.25$ and 0.75). That phase interval—corresponding to velocity shifts of the two stars within 90% of their full amplitudes—maximizes the sample of images while minimizing "velocity blur." We combined the individual profiles, weighting each by a characteristic flux variance, and calculated a weighted rms to evaluate the dispersion of the individual line shapes about the mean.

Figure 6 compares co-added profiles from the 1980 epoch to those obtained over the 5 year period 1981.0–1986.1, including also profiles within ± 0.05 cycles of the two conjunctions ($\phi = 0.00$ and 0.50). Compared with the 1981–1986 collection the earlier profiles show an enhanced blue peak at $\phi = 0.25$, a (unaccountably) depressed red peak at $\phi = 0.00/0.50$, and essentially no difference at $\phi = 0.75$. The red/blue peak asymmetry of the 1980 profiles is similar to that of the $\phi = 0.29$ spectra taken in 1989 January and the $\phi = 0.20$ and 0.27 spectra taken in 1992 February. The average $\phi = 0.25$ profile over the 1981–1986 interval is closer to that recorded by the GHRS in 1991 April at $\phi = 0.26$.

Because our ultimate goal was to assist in the interpretation of the unique GHRS ECH-A spectrum we further restricted the reference profiles to the intermediate epoch (1981.0–1986.1) when the $\phi \approx 0.25$ line shape was most *Hubble*-like. Of the 120 original spectra, 13 remained for $\phi = 0.25$ and only four for $\phi = 0.75$. The resulting co-added profiles are compared in Figure 7 with a smoothed version of the GHRS profile (normalized to the peak flux of the *IUE* profile at $\phi = 0.25$). The match between the $\phi = 0.25$ *IUE* co-added profile and the $\phi = 0.26$ GHRS profile is tolerably good, given the apparent spread in the *IUE* line shapes (particularly in the blue peak and wing). The $\phi = 0.75$ profile exhibits a small redshift with respect to $\phi = 0.25$, the blue peak is sharper, while the red peak

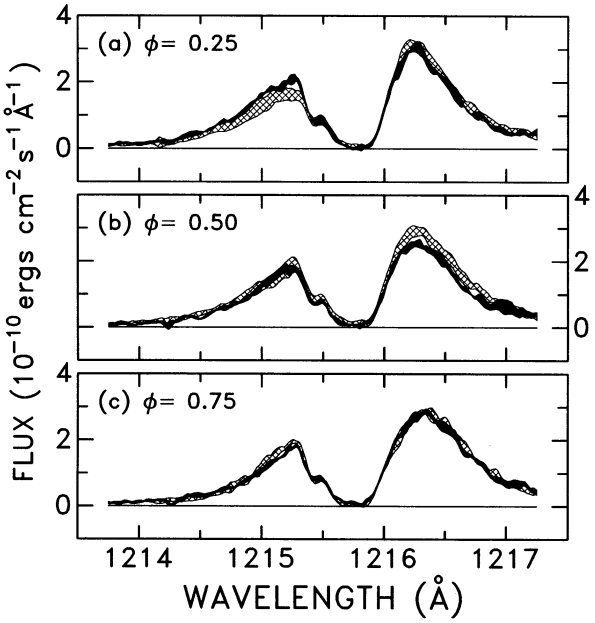

FIG. 6.—Comparison of co-added profiles of Lyα from two epochs: *dark shaded*, early 1980; *light shaded*, 1981–1986. The width of the shading indicates the rms of the weighted sum. The SWP sensitivity degradation has been compensated as described in the text. The 1980 data were obtained during three 8 hr observing sessions spaced about 26 days apart at critical orbital phases. The other observations were obtained during several programs dispersed in phase and time over the 5 year period. The 1980 $\phi = 0.25$ profile shows a distinctly elevated blue peak compared with the mean profile of the later period; the $\phi = 0.50$ profile has a curiously depressed red peak; but the $\phi = 0.75$ profile is essentially identical to that of the later period.

is somewhat broader. These characteristics provide a basis for dissecting the intrinsic line shapes of the two components of the Capella system.

Notice also that the D I absorption of the co-added *IUE* profile at $\phi = 0.25$ lies slightly above that of the smoothed

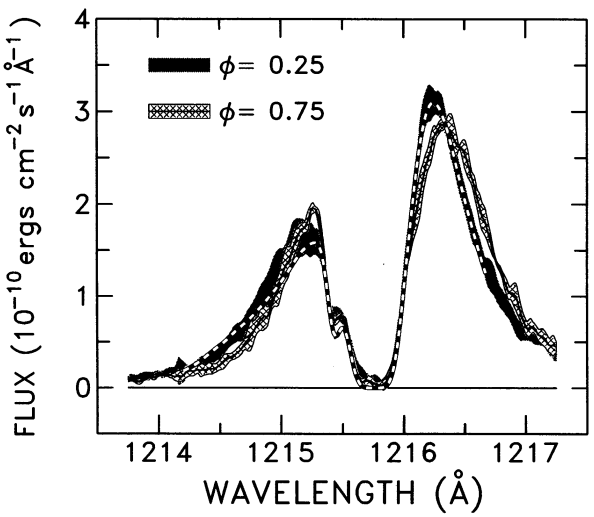

FIG. 7.—Co-added Lyα profiles (*shaded*) from 1981–1986 period compared with the $\phi = 0.26$ GHRS observation (*heavy dashed*) smoothed to the *IUE* resolution and normalized in flux to the peak of the *IUE* $\phi = 0.25$ profile. While the agreement between the *IUE* and GHRS profiles is good (at $\phi = 0.25$), note that the D I absorption in the *IUE* profile lies slightly above that of the ECH-A. We can improve the agreement by subtracting an additional "scattered light" level from the *IUE* spectra.

GHRS profile. The probable cause of the discrepancy is *in-order* scattered light that is not compensated by our background correction. We therefore subtracted a uniform 0.2×10^{-10} ergs cm^{-2} s^{-1} Å^{-1} (i.e., $\approx$7% of the red-peak flux) from the *IUE* profiles at both phases to produce a more *Hubble*-like absorption core.

3. ANALYSIS: DISSECTION OF THE COMPOSITE PROFILES

As described in the companion paper by Linsky et al. (1993) the high resolution and high S/N of the GHRS Lyα profile permit one to recover the intrinsic line shape (for an assumed column density of H I) by deconvolving the predicted interstellar absorption from the observed profile. Modeling the *IUE* line shapes at the opposite phases $\phi = 0.25$ and 0.75 then provides sufficient constraints on the intrinsic stellar profiles to isolate which "dereddened" HST composite profile (at $\phi = 0.26$) is most consistent. Thus the independent *IUE* and *HST* data sets cooperate to reveal N_H. One approach to the *HST-IUE* modeling is presented here. A complementary approach—based on scaled solar Lyα profiles—is presented in the companion paper.

3.1. *Modeling the Opposite Quadratures*

We model the line profiles of each of the Capella stars by piecewise linear segments arranged to mimic the centrally reversed core and damping wings of the hypothetical Lyα emission. We smooth the segmented profiles with Gaussians of FWHM = 10 and 60 km s^{-1}, respectively, to simulate the rotational broadening of the G8 III and G0 III components ($v \sin i \approx 6$ and 36 km s^{-1}). We shift the model profiles by the appropriate radial velocities at the opposite phases (Batten et al. 1991) and combine them. To facilitate comparisons with the observed profiles, we attenuate the composite profile by the interstellar D I + H I absorption for a reference N_H using the temperature and nonthermal broadening of the ISM gas deduced by Linsky et al. (1993). We place the local ISM at a radial velocity of -9.5 km s^{-1} relative to the center-of-mass frame of the Capella system based on the absolute velocities of the D I, Fe II, and Mg II absorptions measured during the *Hubble* program. We adopt Morton's (1991) values of the wavelengths, oscillator strengths, and radiation damping constants of the D I and H I multiplets. We smooth the attenuated composite profile to the 25 km s^{-1} *IUE* resolution and then iteratively modify the intrinsic line shapes until we reproduce the observed profiles at both orbital quadratures. Figure 8 illustrates the final models for $N_H = 1.8 \times 10^{18}$ cm^{-2} (the "best-fit" value derived in the companion paper).

The fact that the observed line shape exhibits a shift to longer wavelengths from $\phi = 0.25$ to 0.75 indicates that the active G0 III star dominates the composite Lyα flux. Note that the blue peak and wing at $\phi = 0.25$ come almost exclusively from the G0 III star, as do the red peak and wing at $\phi = 0.75$. Thus the observed features heavily constrain the overall shape of the G0 III profile; whatever remains must be due to the less-active G8 III star. The inferred profile for the G8 III component is narrow and relatively symmetric, whereas the G0 III component is broad and asymmetric. Both profiles have distinct central reversals. These attributes are insensitive to the assumed hydrogen column over the range of values we consider most plausible.

The portion of the line profile that is most sensitive to the hydrogen column is the red edge of the absorption core. The main contribution to the profile near the red edge at $\phi = 0.25$ is the blueshifted red peak of the G0 III component. That portion of the G0 III profile is "unveiled" from behind the ISM at $\phi = 0.75$ by the $\approx$55 km s^{-1} shift of the G0 III star. Thus the red peak of the $\phi = 0.75$ profile strongly constrains the appearance of the $\phi = 0.25$ intrinsic profile at the red edge of the ISM absorption core.

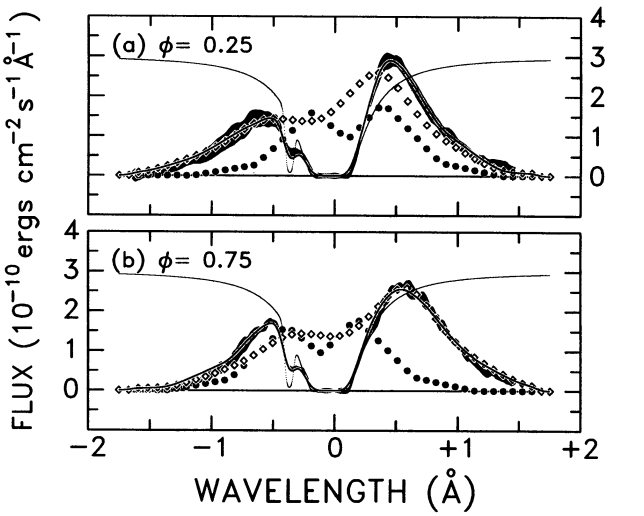

FIG. 8.—Simulation of the Lyα features of the two giants of Capella at opposite orbital quadratures: (*a*) $\phi = 0.25$ when the active G0 III star (*diamonds*) is shifted to the blue and the less active G8 III star (*dots*) to the red; (*b*) $\phi = 0.75$ when the G0 III star is shifted to the red and the G8 III star to the blue. The observed profiles, corrected for the additional scattered light level, are shaded; the thin curves indicate the predicted interstellar D I + H I absorption (for $N_H = 1.8 \times 10^{18}$ cm^{-2}); and the heavy solid curves are the sum of the rotationally broadened stellar profiles attenuated by the interstellar absorption and smoothed to the 25 km s^{-1} *IUE* resolution. Note that the blue wing of the composite profile at $\phi = 0.25$ and the red wing at $\phi = 0.75$ are almost completely dominated by the broad asymmetric G0 III component. The influence of the narrower more symmetric G8 III feature is restricted to the red and blue peaks, respectively, at $\phi = 0.25$ and 0.75.

The central reversal of the G8 III component also affects the overall Lyα profile at $\phi = 0.25$ in the small wavelength interval that most sensitively indicates N_H. The best matches we obtained to the co-added $\phi = 0.25$ *IUE* profile require a moderate ($\approx$50%) central reversal of the G8 III component. Unfortunately, the core of the narrow G8 III profile is completely obscured by the ISM absorption at $\phi = 0.75$.

Very little is known concerning the true appearance of the Lyα emission of any star except the Sun. Neff et al. (1990) did succeed in extracting the red peak of the Lyα emission of δ Lep, a high-velocity G8 giant. A dereddened and symmetrized version of the Lyα profile of δ Lep indicates a central reversal of as much as 50% of the red peak. While the Capella G8 III star is the same spectral type, it is a more active giant than δ Lep (cf. Ayres 1988) and thus might have a significantly different Lyα shape.

3.2. *Comparison with* Mg II

Neff et al. (1990) were surprised to find that the Lyα profile of δ Lep is nearly identical to its chromospheric Mg II λ2795 *k* line. Perhaps, then, the Mg II line shapes of the Capella stars can serve as proxies for their partially or wholly masked Lyα reversals.

Figure 9 depicts a dissection of the MgII *k*-line profile of Capella based on $\phi = 0.29$ and 0.75 LWP-HI echellograms obtained in late 1988 and early 1989 (e.g., Ayres 1991b). We removed the ISM absorption from the observed profiles using

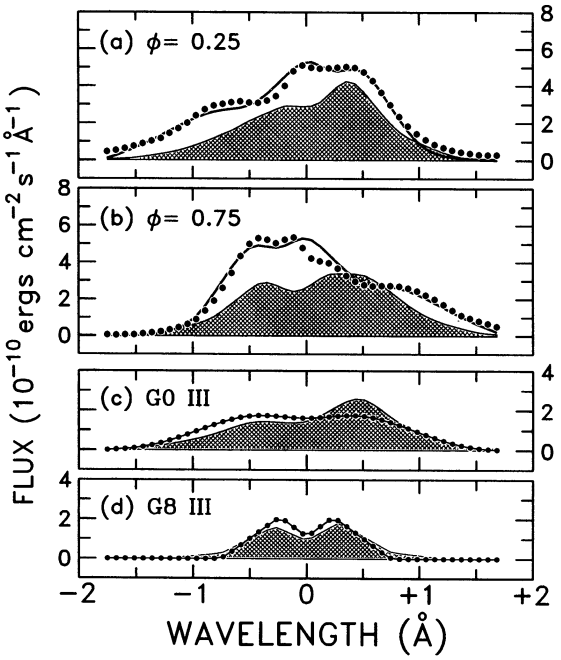

FIG. 9.—Comparison of the derived Lyα line shapes of the Capella stars with those deduced from the Mg II λ2795 (*k*) resonance line. We have depicted both sets of features on the same Δλ scale as advocated by Neff et al. (1990). In (*a*) and (*b*) we compare the observed *k*-line (*dots*) at $\phi = 0.25$ and 0.75 "dereddened" according to the Mg^+ column reported by Linsky et al. (1993), with the *IUE*-derived intrinsic line shapes of the Lyα feature (for $N_H = 1.8 \times 10^{18}$ cm^{-2}; shaded). The Mg II features have had a "basal" flux of about 0.7×10^{-10} ergs cm^{-2} s^{-1} Å^{-1} subtracted prior to display. Some of that light probably is grating scatter, but most is genuine emission from the stellar chromospheres (cf. Linsky & Ayres 1978). Note that even without the basal contribution the *k*-line emission significantly exceeds that of the H I resonance line (and the total "Mg II" emission would include the companion λ2802 *h* line). The solid curves represent simulated composite profiles obtained in much the same way as the Lyα profiles depicted in Fig. 8. In (*c*) and (*d*) we compare the inferred Mg II *k* (*dots*) and Lyα (*shaded*) line shapes for the two stars separately. The profiles are normalized (to the Lyα flux scale) according to the integrated fluxes. Note that while the composite Mg II and Lyα profiles at the opposite quadratures are only superficially similar, the individual line shapes are remarkably alike in FWHM and depth of the central reversal. A similar correspondence was noted by Neff et al. (1990) for the high-velocity G8 giant δ Lep.

the atomic parameters of Morton (1991) and the properties of the Capella sightline derived by Linsky et al. (1993). As in the Lyα simulations we rotationally smoothed the model profiles of the G8 III and G0 III stars before adding them. The figure also compares the derived intrinsic *k*-line profiles with those of Lyα on the same Δλ scale as advocated by Neff et al. (1990). While the composite profiles at the opposite quadratures are only vaguely similar in appearance, the individual line shapes (when normalized in flux) are nearly identical aside from the asymmetry of the Lyα profile of the G0 III star and the more severe rotational smoothing of its longer-wavelength *k*-line profile.

The curious similarity between the Lyα and Mg II *k*-line profiles of δ Lep and those of the Capella giants might be accidental. On the other hand, a simple scaling of the profiles with Δλ (rather than, say, with *velocity*) is possible if the outer edges of the line shapes are controlled by the Lorentzian wings instead of the Doppler core (see discussion in Ayres 1979). In that event the column density through the lower transition zone ($T_{H\,I} \approx 1$–2×10^4 K) must be smaller than the column density through the chromosphere proper ($T_{Mg\,II} \approx 7 \times 10^3$ K) by approximately the Mg/H abundance ratio. That, in turn, is plausible because the depth of the chromospheric temperature inversion is determined in part by *metal* ionization, whereas the base of the transition-zone temperature rise is determined by the ionization of hydrogen itself (see, e.g., Ayres 1979).

It is less easy to understand, however, why the *central reversals* of the Dopper cores (inside the peaks) of Lyα and *k* would be similar on a Δλ scale. According to arguments presented by Gayley (1992) the similarity in core shapes would imply that the *nonthermal* broadening where the *k*-line forms is similar to the *thermal* broadening where the Lyα core arises. Whether the correspondence between nonthermal motions and temperature is a coincidence or a fundamental aspect of chromospheric structure remains to be clarified.

Thus while we believe that the choice of a 50% central reversal for the Lyα profile of the Capella G8 III star is reasonable, our most compelling evidence is circumstantial. Fortunately even the extremes of a flat-topped profile or a deep reversal to zero intensity have only a small effect on the deduced N_H (Linsky et al. 1993).

4. DISCUSSION

The original intent of our foray into the *IUE* Archives was to help extract a cosmologically useful result from the GHRS observation of the local ISM against the backdrop provided by the chromospheric emissions of Capella. As described in the companion paper (Linsky et al. 1993) our joint analysis succeeded in yielding a secure result for N_H and thus also for the D/H ratio.

At the same time our exploration of the extensive *IUE* data set has revealed what might be significant temporal changes in the Capella Lyα line shape through the *IUE* era. We are cautiously optimistic that we have eliminated obvious instrumental effects and believe that the secular variations in the profiles are real. The most significant changes in the $\phi \approx 0.25$ line shapes occur in the blue wing dominated by the G0 III star. The evolution from the more symmetric line shape of early 1980 to the asymmetric *Hubble*-like profile a year later contrasts sharply with the short-term stability in profiles and/or integrated fluxes noted in two medium-term monitoring programs (early-1981 and early-1986; Ayres 1984, 1991a). Furthermore, our "dissection" indicates that the average profile of the G0 III star must be significantly distorted with a red/blue peak asymmetry of nearly 1.8. The distortion is in the sense of that expected from a 100–200 km s^{-1} outflow of material.

Prior to the *IUE*, Dupree (1975) proposed that the Capella *G8 III star* has a strong stellar wind of moderate excitation ($\approx 3 \times 10^5$ K) based on blueshifted O VI emission in an early *Copernicus* spectrum. However, the O VI emission at that particular orbital phase almost certainly was associated with the blueshifted *G0 III star*, which subsequent *IUE* work showed was responsible for most of the ultraviolet "activity" of the system (Ayres & Linsky 1980).

Nevertheless, Simon & Drake (1989, SD) recently have resurrected the idea of strong winds in the Hertzsprung-gap giants (like the Capella G0 III star). They propose two types of winds during different stages of the coronal development of these moderate-mass (2–3 $M_\odot$) stars during their post–main-sequence phase. The authors hypothesize that the initial crossing into the F-types is dominated by classical-acoustic coronal heating with an unrestrained expansion of hot gas responsible for the curious "X-ray deficiencies" of the F-G0 giants.

However, once the stars reach late-F, their convection zones deepen sufficiently to drive a vigorous "dynamo" like that believed to control the activity of cool main-sequence stars such as the Sun (Parker 1970). The sudden onset of coronal magnetic activity and a solar-like magnetized wind then causes the dramatic slowing of the stellar rotation near G0 in the giant branch (cf. Gray 1991).

The asymmetry of the Lyα profile of the G0 III star places some restrictions on the nature of a wind. The mass-loss rate can be estimated from the hydrogen column required to produce noticeable attenuation of the blue peak. Since the "absorption" is broad ($\Delta\lambda \approx 1$ Å), the wind either has a relatively narrow Doppler profile (i.e., $T \lesssim 2 \times 10^4$ K) while smoothly accelerating from essentially rest to a high terminal velocity (say, $v_\infty \gtrsim 250$ km s^{-1}), or it has a much higher temperature (say, $T > 10^6$ K) and a smaller terminal velocity (say, $v_\infty \approx 120$ km s^{-1}). The column density of atomic hydrogen necessary to achieve line center $\tau = 1$ for a thermally broadened profile is $N_{\rm H} \approx 1.7 \times 10^{13}(T_4)^{1/2}$ cm^{-2}, where T_4 is the wind temperature in units of 10^4 K. The associated column mass is $m_{\rm w} \approx 2.3 \times 10^{-24}(1 + \zeta_p)N_{\rm H} \approx 3.9 \times 10^{-11}(1 + \zeta_p)(T_4)^{1/2}$ g cm^{-2}, where ζ_p is the ratio of protons to neutrals.

We estimate ζ_p by the "coronal" approximation. Taking the $1 \rightarrow \kappa$ collisional ionization coefficient from Vernazza, Avrett, & Loeser (1981) and the radiative recombination rate from Spitzer (1978), we obtain $\zeta_p \approx 1 \times 10^4 T_4^{1.5} \exp(-15.8/T_4)$. The ion fraction ranges from 6×10^4 at 1×10^5 K to 7×10^6 at 1×10^6 K. At lower temperatures the ionization equilibrium cannot be described so glibly (e.g., Athay 1986). Nevertheless it is probable that $\zeta_p \gtrsim 1$ for $T_4 \gtrsim 1$.

The mass-loss rate can be estimated from $\dot{M} \approx 4\pi r m_{\rm w} v_\infty$, where r is the radius at which the flow attains its terminal velocity. If we take $r \approx R_\star \approx 9\ R_\odot$, then we obtain $\dot{M} \approx 1 \times 10^{-12} T_4^2 \exp(-15.8/T_4)(v_\infty/200\ {\rm km\ s^{-1}})\ M_\odot$ yr^{-1} for the high-temperature case ($T > 10^5$ K) and $\dot{M} \gtrsim 1 \times 10^{-16}\ M_\odot$ yr^{-1} for the lower temperatures ($T \gtrsim 10^4$ K).

The mass-loss rate is unimportant in the latter regime. On the other hand, a truly coronal wind (i.e., $T \gtrsim 10^6$ K) will produce a mass-loss rate $\dot{M} \geq 1 \times 10^{-8}\ M_\odot$ yr^{-1}, which is in serious disagreement with the weak radio detections of α Aur by the VLA. The 6 cm flux of about 0.2 mJy—if attributed entirely to an ionized wind—sets a limit of about $7 \times 10^{-10}\ M_\odot$ yr^{-1} on the mass-loss rate (Drake & Linsky 1986).

Nevertheless a moderate-excitation ($\lesssim 1 \times 10^5$ K) magnetized wind with a mass-loss rate as small as $1 \times 10^{-10}\ M_\odot$ yr^{-1} would shed angular momentum at a furious rate compared with the solar coronal wind (whose mass-loss rate of a few $\times 10^{-14}\ M_\odot$ yr^{-1} leads to a spindown time of about 1 Gyr; SD and references therein). A factor of only 10^3 reduction in the solar braking time scale can explain the sudden drop in rotational velocity at G0 in the Hertzsprung gap (e.g., SD). Furthermore, the existence of such a wind might explain the surprising lack of He II λ304 emission from Capella noted in a recent EUV sounding-rocket flight (Green et al. 1992), and the curious phase-dependent He I λ10830 absorption profile of the G8 III star, which also apparently is modulated at the rotational period of the G0 III star (Katsova 1992).

While the discovery of a distorted and variable Lyα emission profile in the archetype UV-active Hertzsprung-gap yellow giant could be viewed as an awkward development, at least for those of us who have believed that "chromospheric winds" are the primary signature of red giants in the coronal graveyard (cf. Linsky & Haisch 1979; Ayres, Fleming, & Schmitt 1991), the observation undoubtedly is a key clue in elucidating the chromospheric/coronal heating mechanism in that crucial transition class in the H-R diagram. For that reason we eagerly await additional far-UV spectroscopy of Capella and other Hertzsprung-gap stars with the first-order gratings of the *Hubble* GHRS.

This work was supported by the National Aeronautics and Space Administration through grants NAG5-199, NAG5-1215, NAGW-2904, and GO-2485.01-87A to the University of Colorado, and S-56500 to the National Institute of Standards and Technology. We also thank A. Diplas for his advice concerning the simulation of the ISM absorption.

REFERENCES

Athay, R. G. 1986, ApJ, 308, 975
Ayres, T. R. 1979, ApJ, 228, 509
———. 1984, ApJ, 284, 784
———. 1988, ApJ, 331, 467
———. 1991a, ApJ, 375, 704
———. 1991b, in The First Year of *HST* Observations, ed. A. L. Kinney & J. C. Blades (Baltimore: STScI), 216
———. 1993, in preparation
Ayres, T. R., Fleming, T. A., & Schmitt, J. H. M. M. 1991, ApJ, 376, L45
Ayres, T. R., Lenz, D., Burton, R., & Bennett, J. 1993, in Proc. 2d Conf. on Astronomical Data Analysis Software and Systems, ed. R. Hanisch, R. Brissenden, & J. Barnes (PASP Conf. Ser.), in press
Ayres, T. R., & Linsky, J. L. 1980, ApJ, 241, 279
Ayres, T. R., Schiffer, F. H., III, & Linsky, J. L. 1983, ApJ, 272, 223
Bagnuolo, W. G., Jr., & Sowell, J. R. 1988, AJ, 96, 1056
Batten, A. H., Hill, G., & Lu, W. 1991, PASP, 103, 623
Bohlin, R. C., & Grillmair, C. J. 1988, ApJS, 66, 209
Drake, S. A., & Linsky, J. L. 1986, AJ, 91, 602
Dupree, A. K. 1975, ApJ, 200, L27
Gayley, K. G. 1992, ApJ, 390, 573
Grady, C. A., & Garhart, M. P. 1989, NASA *IUE* Newsletter, 37, 102
Gray, D. F. 1991, in Angular Momentum Evolution of Young Stars, ed. S. Catalano & J. R. Stauffer (Dordrecht: Kluwer), 183
Green, J. C., Wilkinson, E., Ayres, T. R., & Cash, W. C. 1992, ApJ, 397, L99
Katsova, M. M. 1992, in Surface Inhomogeneities on Late-Type Stars, ed. P. B. Byrne & D. J. Mullan (Berlin: Springer), 220
Kinney, A. L., Bohlin, R. C., & Neill, J. D. 1991, PASP, 103, 694
Linsky, J. L., & Ayres, T. R. 1978, ApJ, 220, 619
Linsky, J. L., Brown, A., Gayley, K., Diplas, A., Savage, B. D., Ayres, T. R., Landsman, W., Shore, S. N., & Heap, S. R. 1993, ApJ, 402, 00
Linsky, J. L., & Haisch, B. M. 1979, ApJ, 229, L27
Morton, D. C. 1991, ApJS, 77, 119
Neff, J. E., Landsman, W. B., Bookbinder, J. A., & Linsky, J. L. 1990, in Evolution in Astrophysics (ESA SP-310), 341
O'Brien, P. T., Rees, P. C. T., & Howarth, I. D. 1990, A Study of the *IUE* Ripple Correction, unpublished report to *IUE* Final Archive Definition Committee
Parker, E. N. 1970, ARA&A, 8, 1
Reader, J., Acquista, N., Sansonetti, C. J., & Sansonetti, J. E. 1990, ApJS, 72, 831
Simon, T., & Drake, S. A. 1989, ApJ, 346, 303 (SD)
Spitzer, L., Jr. 1978, Physical Processes in the Interstellar Medium (New York: Wiley), 107
Vernazza, J. E., Avrett, E. H., & Loeser, R. 1981, ApJS, 45, 635